Chapter 10
Novel Imaging Techniques: Polarized Neutrons and Neutron-Based Magnetic Resonance Imaging

N. Kardjilov, W.T.H. Lee, and G.E. Granroth

Abstract This chapter describes three rather novel neutron-based imaging methods all of which involve magnetic fields. The first two take advantage of the neutron magnetic moment which makes it sensitive to the presence of magnetic fields. In the first application the Larmor precession of the neutron in a magnetic field is used to produce two- and three-dimensional (3D) visualization of magnetic field distributions in free space and in bulk materials.

In the second potential application, the Larmor precession is used as a measure of the material density through which the beam passes. Although this technique of spin contrast imaging is still very much in the concept stage, initial estimates show that it is feasible with new sources and may open up the possibility of obtaining 3D images without moving the sample.

Polarization of the nuclei in a material can also provide unique ways of imaging a system. By partially polarizing the nuclei with a sufficiently large magnetic field, the Zeeman splitting of the nuclei can be detected by high-resolution neutron spectroscopy. If the field is then reduced, the time for the Zeeman splitting to relax to the equilibrium value is a measure of the nuclear relaxation time; this is the physical quantity measured in magnetic resonance imaging. A full image of the relaxation times with respect to position could then be obtained by rastering the sample in the neutron beam.

Keywords Polarized neutrons · Magnetic fields · Magnetic resonance imaging · Spin-echo · Time-of-flight · three-dimensional imaging

10.1 Neutron Spin Polarized Imaging of Magnetic Field

Neutrons are sensitive to magnetic fields due to their magnetic moment, i.e., spin. Therefore, similar to the conventional attenuation contrast image, the magnetic field inside and around a sample can be visualized independently by detection of

N. Kardjilov (✉)
Helmholtz Centre Berlin for Materials and Energy, Berlin, Germany
e-mail: kardjilov@helmholtz-berlin.de

I.S. Anderson et al. (eds.), *Neutron Imaging and Applications*,
Neutron Scattering Applications and Techniques, DOI 10.1007/978-0-387-78693-3_10,

the polarization changes in the transmitted beam. Polarized neutron radiography is based on the spatially resolved measurement of the final precession angles of a collimated and polarized monochromatic neutron beam that is transmitted through the magnetic field, which is present inside and outside of a sample.

This new technique can be described using theoretical considerations related to the interaction of the magnetic moment of the neutron with the magnetic field. In the presence of a magnetic field $\vec{B}$, the magnetic moment (i.e., the spin $\vec{S}$) of the neutron will perform Larmor precession with a frequency ω_L. For a monochromatic neutron beam having a uniform neutron velocity v, the precession angle φ is proportional to the integral of the magnetic field $\vec{B}$ along a certain path:

$$\varphi = \omega_L t = \frac{\gamma_L}{v} \int_{path} B ds \tag{10.1}$$

where γ_L is the neutron gyromagnetic ratio. φ can be measured experimentally using a spin polarizer-analyzer arrangement as shown in Fig. 10.1. Here the neutrons are first polarized (Chapter 3) and, after the interaction with the magnetic field, the final spin orientation is analyzed with respect to the initial state. The signal transmitted through the spin analyzer depends on the spin rotation angle (Eq. 10.1) and has a maximum for parallel and a minimum for anti-parallel spin orientation. In this case the detected image behind the analyzer is determined by a superposition of conventional attenuation contrast $I_a(x,y)$ and the contrast variations due to spin rotation $I_m(x,y)$:

$$I(x,y) = \underbrace{I_0(x,y) \cdot \exp(-\int_{path} \Sigma(s) ds)}_{I_a(x,y)} \cdot \underbrace{\frac{1}{2}(1 + \cos\varphi(x,y))}_{I_m(x,y)} \tag{10.2}$$

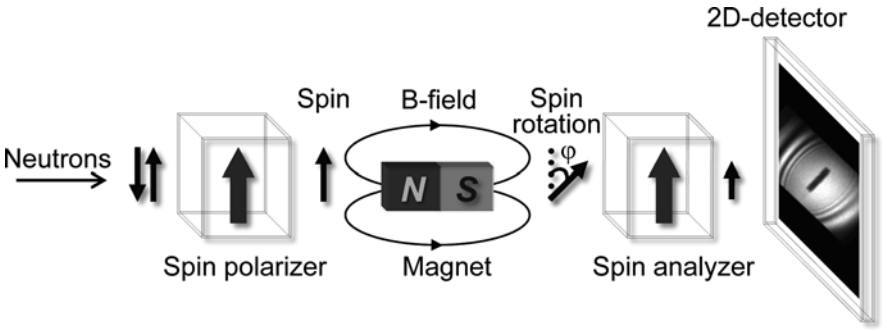

Fig. 10.1 Schematic of the set-up used for imaging magnetic materials on CONRAD. The neutron beam is first polarized, then precesses around a magnetic field is analyzed and finally detected. Note how the intensity (represented by the height of the *dark arrow*) behind the analyzer is smaller than the intensity behind the polarizer [1]

where $I_0(x,y)$ is the incident beam intensity, $\Sigma(x,y)$ is the linear attenuation coefficient of the sample and (x,y) are the coordinates in the detector plane. The cosine implies a periodic transmission function for the analyzed precession angles and complicates a straightforward quantification with respect to the traversed magnetic fields. By use of a calculation model based on the Biot-Savart law, it was shown that quantitative analysis is possible [1].

Imaging experiments using the setup shown in Fig. 10.1 were carried out at the neutron tomography facility CONRAD at HMI [1]. For this purpose the instrument was equipped with solid-state polarizing benders [2] providing a beam with a cross-section of 15 mm width and 45 mm height. For investigation of larger samples, up to 20 cm width, a scanning arrangement was adapted. A double crystal monochromator [3] was used to select a defined wavelength from the cold neutron spectrum. The spatial resolution achieved in the radiography images was around 500 μm for the given experimental geometry.

The potential of the method was demonstrated by visualization of the magnetic field around a simple dipole magnet (Fig. 10.2). This shows the

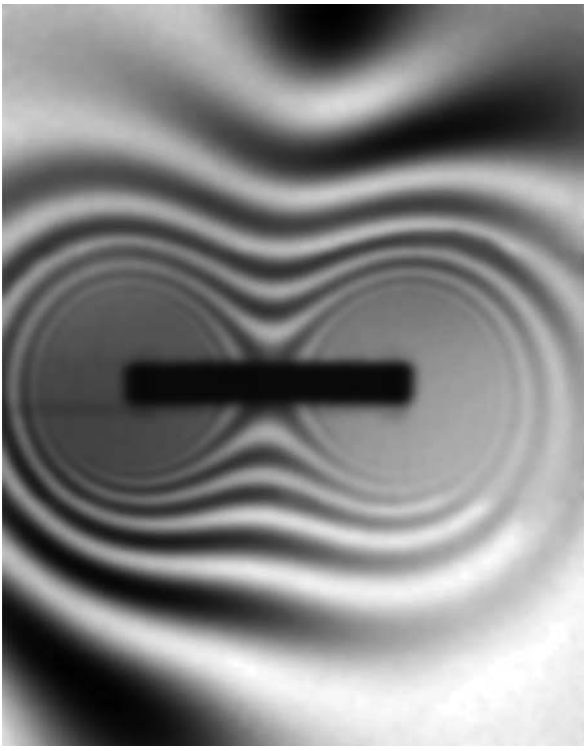

Fig. 10.2 A radiograph showing the field lines surrounding a bar magnet. The magnetic field decreases in strength with distance from the magnet, resulting in a series of maxima and minima, where the beam polarization is sequentially parallel or antiparallel to the analyzer. Very close to the magnets (where the field is strongest) the field lines are too close together to be spatially resolved

decay of the magnetic field strength with increasing distance from the magnet, resulting in an annular structure around the sample with an increasing period due to the changing precession angles of the neutron spins on their path through the strongly decaying field. The gray level scale used in the images is related to the intensity variations induced by the sample and the magnetic field (from black = minimum to white = maximum, representing the periodic 2π rotation of the neutron spin). The structure in the center part cannot be seen due to the limited spatial resolution of approximately 500 μm [4].

This imaging method can in some instances be extended into three dimensions by a standard tomographic technique. Figure 10.3 shows the distribution of a magnetic field trapped inside a polycrystalline lead cylinder, with a diameter of 1 cm and length of 3 cm, that becomes superconducting when cooled below the critical temperature, T_c = 7.2 K. The sample was cooled down to 6.8 K in a homogenous magnetic field of 10 mT. After this the magnetic field was switched off, resulting in partially trapped magnetic fields in the

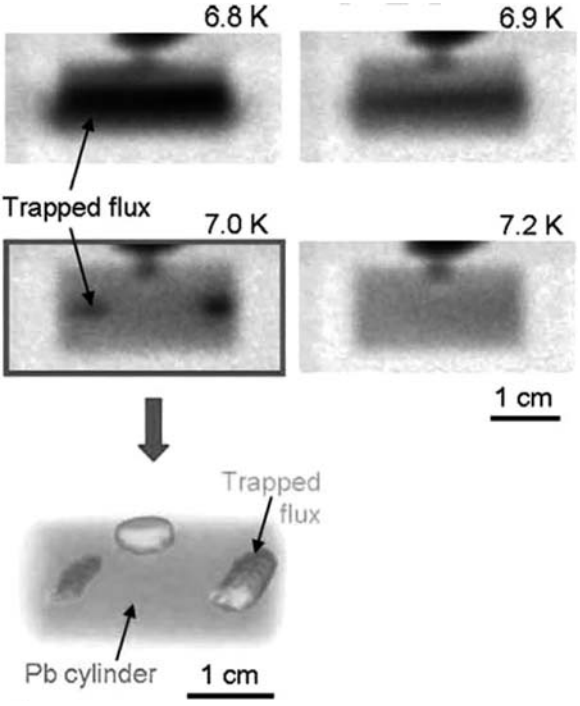

Fig. 10.3 A 3D reconstruction of trapped flux (solid regions left and right) inside a polycrystalline cylinder of lead. When cooled to below its critical temperature (7.2 K) in the presence of a weak magnetic field, some flux is present inside due to defects and grain boundaries and this remains trapped even after the field is switched off [1]

superconductor due to grain boundaries and other defects [5, 6]. The temperature dependence of the residual field distribution inside the sample was visualized by recording radiographic images during the heating process. The images (Fig. 10.3) show an inhomogeneous residual field which decreases during heating and vanishes completely when the critical temperature T_c is reached. For the weak trapped residual field at 7.0 K, a tomographic investigation was performed by rotating the sample around its vertical axis. The beam attenuation for each pixel can be related to absorption and magnetic contrast (Eq. 10.2) assuming that the trapped magnetic field conserves its main orientation perpendicular to the beam polarization and is weak enough to cause spin rotations smaller than π for all recorded projections. The volumetric data set was reconstructed from 60 2D images, collected through rotation over 180°, using a filtered back projection algorithm (Chapter 6). The results show the three-dimensional (3D) representation of the flux trapped in the sample. Flux concentrations could be found close to the end surfaces of the cylinder and at the position where the sample was held with a screw.

This imaging method has many potential applications. The presence and controlled application of magnetic fields are essential in many fields of science and technology as well as in fundamental physics. For example, the flux distribution and flux pinning in large superconducting samples, the skin effect [7] in conductors, or magnetic domain distributions in bulk ferromagnets could be visualized and studied in detail.

10.2 Spin Echo Imaging

The Larmor precession described in the previous section forms the base of the neutron spin-echo technique which is typically used to determine small energy or momentum changes upon scattering [7], see also Neutron Scattering Instrumentation [8]. In a typical spin-echo setup (Fig. 10.4), two identical regions of magnetic field are applied before and after a "π-flipper." A neutron with polarization perpendicular to the field undergoes Larmor precession in the first field region and its spin rotates by an angle of ϕ radians. Due to the energy spread of the neutron beam, the spins of different energy neutrons acquire different precession angles and the neutron beam appears to be depolarized after the first field region. The π-flipper between the two magnetic field regions rotates the neutron spins about an axis perpendicular to the applied field by 180°. This has the effect of reversing the angle of the neutron spin from ϕ to $-\phi$. Since the two magnetic field regions are identical, the neutron spin rotates an additional angle of ϕ radians in the second field region. The spin precession in the two field regions cancels and the beam "recovers" its polarization after going through the field regions. This setup constitutes a neutron spin-echo instrument, and the process through which the neutron beam recovers its polarization is called "spin echo."

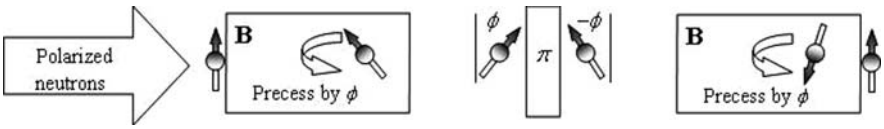

Fig. 10.4 A basic neutron spin-echo instrument setup. The spin of a neutron undergoes Larmor precession in the upstream magnetic field. A π-flipper between the magnetic field regions inverted the spin rotation angle from θ to $-\theta$. The neutron spin rotates an additional angle equal to θ in the identical downstream field region and returns to its starting direction

In neutron spin-echo spectrometers, a sample is placed between the two magnetic field regions in the neutron flight path. Inelastic scattering of the neutron beam changes the energy (velocity) of the neutrons, so that the times that a neutron spends in the two field regions are no longer equal. Since the spin precession is proportional to the time spent in the magnetic field, this prevents the beam from completely recovering its polarization. The rate of depolarization is proportional to the difference in the times spent in the two field regions; hence the neutron energy change due to inelastic scattering by the sample can be determined.

In a previous development [9], experiments were carried out to measure the neutron optical potential in nonmagnetic materials by applying the neutron spin-echo technique. When a neutron beam goes through a material without being scattered, it experiences an optical potential and changes its momentum. In neutron optics, the optical potential manifests as the neutron index of refraction n,

$$n = 1 - \frac{Nb\lambda^2}{2\pi} \ , \tag{10.3}$$

where N is the number density of the material, b is the coherent scattering length, and λ is the neutron wavelength. The velocity of a neutron in the material is related to its velocity in vacuum v_0 by $v = nv_0$. Due to the change in the neutron velocity, neutrons that go through a material along a direction x over a distance X acquire an additional spin angle ϕ, given by

$$\phi = \int_0^X \gamma_{\mathrm{L}} B \frac{1}{n(x)v_0} dx - \int_0^X \gamma_{\mathrm{L}} B \frac{1}{v_0} dx = \frac{m_n \gamma_L}{2\pi h} B\lambda^3 \int_0^X N(x)b(x)dx \ , \tag{10.4}$$

where m_{n} is the neutron mass, h is the Planck's constant, and b is the coherent scattering length. The quantity $N(x)b(x)$ is more commonly known as the neutron scattering length density. The magnitude of the neutron scattering length density ranges from 10^{-7} Å^{-2} to 10^{-5} Å^{-2}. Hence the spin angle change ϕ measures the path integral of the scattering length density.

In a modification of the neutron spin-echo instrument discussed above, placing a material in one arm of the pair of magnetic field regions results in a

net neutron spin angle that corresponds to the path integral of the scattering length density. With a proper neutron beam arrangement, this effect can be applied to measure the optical potential as a function of position in a material – an imaging technique. A typical benchmark for an imaging technique is a 1 mm spatial resolution. A common neutron polarization analyzer such as a polarized ^{3}He analyzer (Chapter 3 in this book) may resolve a spin angle of 10°. If the magnetic field strength is strong enough to rotate the neutron spin by 10° over 1 mm of its flight path, a 1 mm imaging resolution in the direction along the beam path can be achieved. Using a typical scattering length density of $Nb = 10^{-6}$ Å^{-2}, Fig. 10.5 shows the magnetic field required to reach $\phi = 10°$ over a 1 mm flight path as a function of the wavelength. A potential imaging device using this spin-echo technique would therefore use cold neutrons with wavelengths ranging from 20 to 100Å and an applied field from several gauss for 100Å neutrons to 1 Tesla for 30Å neutrons. The magnetic potential energy $U = -\vec{\mu} \cdot \vec{B}$, where $\bar{\mu}$ is the neutron magnetic moment, is equal to 0.06 μeV in a 1 Tesla field. Hence, compared with a kinetic energy of 8.181 μeV for 100Å neutrons, the optical effect of the magnetic potential can be ignored.

One main difference between the imaging application and the neutron spin-echo spectrometer is that in imaging, the additional change in the spin angle occurs only when the neutron is inside the material, whereas the change accumulates over the entire field region after the sample in the case of spin echo spectrometer. This makes the spin angle change insensitive to the beam divergence. The beam divergence, however, is still important in that neutrons through different parts of a sample may end up striking the same detector pixel. This blurring of the image is, however, a common concern for all imaging

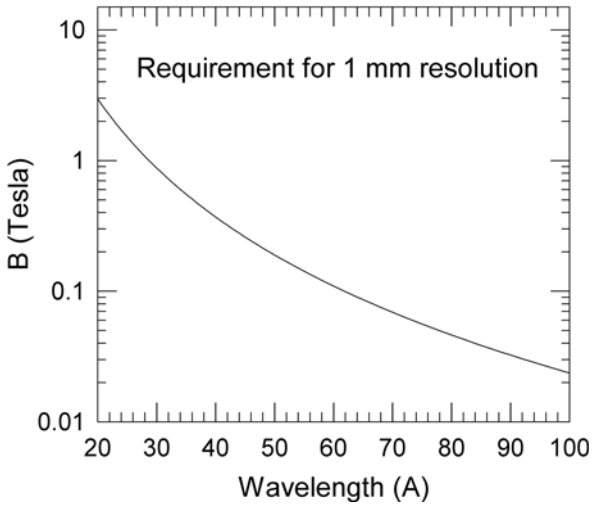

Fig. 10.5 Applied field strength necessary to achieve a 1 mm resolution

techniques rather than being specific to the spin contrast imaging. In neutron imaging, collimation is used to reduce the divergence and anti-grids can be used between the sample and the detector system. The same setup can be applied in the techniques discussed here.

To acquire a three-dimensional image of an object using imaging techniques based on direct neutron absorption, measurements with the neutron beam passing the object at different angles are first carried out and tomography reconstruction is then applied to render the 3D image. The advantage of the imaging technique discussed here is that it can be used with a time-of-flight (TOF) technique to achieve 3D imaging without the need to measure the object at many different angles and without using tomographic reconstruction.

The idea behind the technique is illustrated in Fig. 10.6. Initially the neutron spins are aligned parallel to the applied field. At time $t = 0$, a $\pi/2$ pulse is applied over the length of the sample to rotate the neutron spins to a perpendicular direction with respect to the field, which starts the precession of the neutron spins. Along the neutron flight path, neutrons at different position along a flight path go through a different path length through the material and therefore acquire a different spin angle change ϕ. For instance, the spin change angle is ϕ_1 for neutrons starting at point 1 and ϕ_2 for neutrons starting at point 2, respectively. The spin angle change is converted to intensity change by a polarization analyzer before the detector. Since neutrons at point 1 at $t = 0$ reach the detector later than neutrons at point 2 at $t = 0$, by recording the time-of-flight of each neutron at the detector, the position of each neutron at $t = 0$ can be determined. Subtracting ϕ_2 from ϕ_2 gives the spin angle change that corresponds to the scattering length density from point 1 to point 2. Applying this analysis to a series of images taken at consecutive times-of-flight, a slice-by-slice 3D distribution of the scattering length density of an object can be obtained. The speed of 30Å neutrons is 131.87 m/s. It takes 7.6 μs to travel a distance of 1 mm. A timing resolution of 1 μs would be sufficient to resolve the initial location of the neutrons at the time the precession is started.

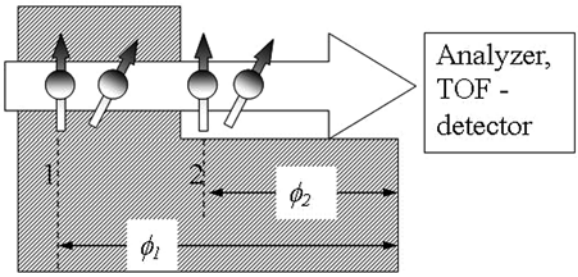

Fig. 10.6 Technique for direct 3D imaging. At time $t = 0$, a $\pi/2$ flip starts the neutron precession; neutrons at point 1 precess through a longer path in the sample than neutrons at point 2. Subtracting the two gives the precession angle from point 1 to point 2

In order to demonstrate the technique, a Monte Carlo simulation was carried out that takes into account bandwidth, beam divergence, and placements of the neutron source and neutron detectors. The sample model is a 1 × 1 cm plate. It is 2 mm thick in the beam direction with one-quarter of the sample cross-section only 1 mm thick. A nominal scattering length density $Nb = 10^{-6}$ Å^{-2}was used for the calculations. The field strength at the sample was 1 Tesla. For the purposes of the simulation a 5 mm diameter, isotropic neutron source located at 4 m from the sample was assumed to produce a 30Å neutron beam with a typical wavelength spread $\Delta\lambda/\lambda = 10\%$. This wavelength spread allows for both 1 mm resolution and sufficient neutron intensity. A detector was located 1m away from the sample. For simplicity, only the additional amount of spin precession in the material was computed instead of the spin precessions in the two magnetic field regions. Also for simplicity, the incident neutron polarization efficiency was assumed to be 1 and the efficiency of the polarization analyzer was also considered to be ideal. In a real instrument, the polarization and the efficiency of the analyzer is typically 95–98%. The neutron intensity after the analyzer is given by $I = \cos^2(\phi)$. In this setup, $\phi \sim 11.5^\circ$ for a passage of 1 mm through the material.

The intensity profile at the image plate detector for different TOF neutrons is shown in Fig. 10.7. The upper-right corner is the region where the material is thinner (1 mm thick compared with 2 mm for the rest of the sample). In Fig. 10.7(a), the neutrons began to precess before entering the sample. In Fig 10.7(b), the neutrons are half-way through the sample when the precession begins. Due to the finite size of the source and the beam divergence, there is blurring of the edges of the modeled sample. The diverging beam also gives rise to an amplified image. To further evaluate the simulation results, the intensity across the x-direction of the image plate at $y = +3$ mm to $+3.2$ mm was extracted to calculate the spin angle change ϕ. The intensity results are shown in Fig. 10.7(c) and the spin angle change results are shown in Fig. 10.7(d). The simulation verifies that $\phi \sim 23^\circ$ for neutrons passing the 2 mm thick area and $\phi \sim 11.5^\circ$ for those passing the 10 mm thick area. Subtracting the two spin angle changes gives the spin angle change through the first 1 mm thick area and it gives the expected $\phi \sim 11.5^\circ$ as shown in Fig. 10.7(d). This demonstrates that, by extracting the spin angle change ϕ from the intensity map at different TOFs, the distribution of the scattering length density in an object can be mapped in a slice-by-slice fashion to give a 3D rendering of the composition.

There are several technological challenges to reaching 1 mm resolution with this method. The first is the requirement to flip the neutron spins by $\pi/2$, i.e., from being parallel to being perpendicular to the 1 Tesla field. The Larmor precession frequency for a 1T field is 29.164 MHz. The neutron spin will rotate 90° in 8.6 ns. To avoid a broadening of the radio-frequency pulse spectrum, a pulse of $2\,n\pi + \pi/2$ can be used. However, a setup accurate to 0.5 ns in the application of the pulse is needed to reach accuracy better than 5° in the $\pi/2$-flipping. A second challenge is the precision required to cancel the spin precession (the spin-echo point) using

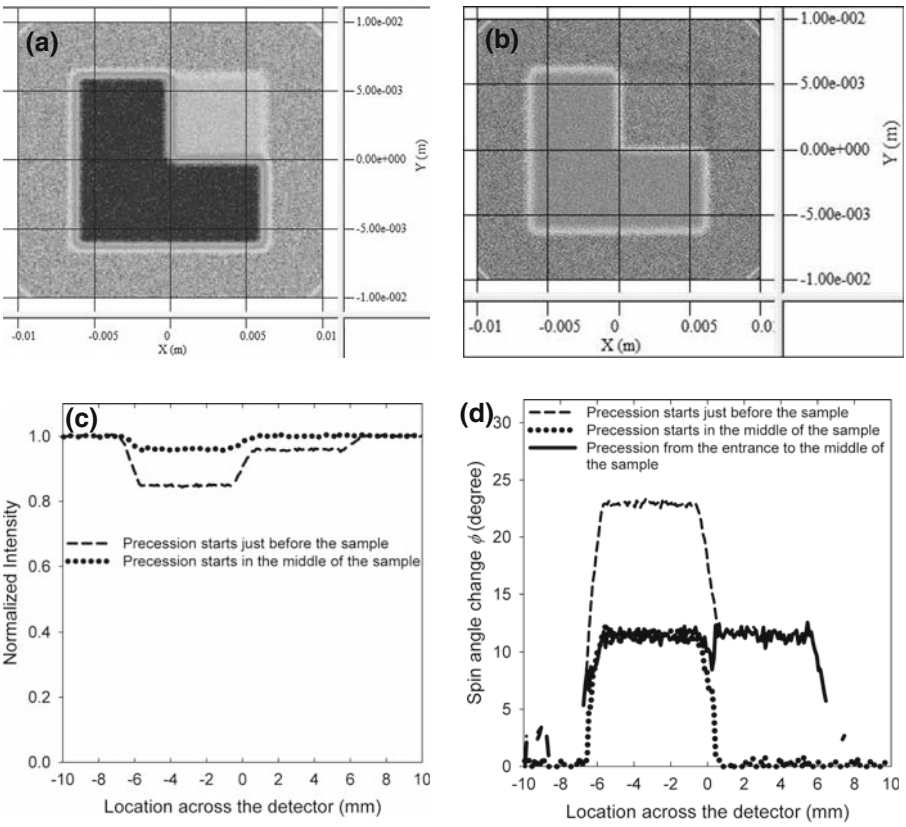

Fig. 10.7 Neutron intensities at the detector if spin precession starts (**a**) when the neutrons are right before the sample, and (**b**) when the neutrons are passing the middle of the sample. The color scales are relative; (**c**) The normalized integrated intensity at the detector along the x-direction of the detector from $y = +2$ mm to $y = +3$ mm from the two detector images shown in (a) and (b); (**d**) The spin angle change ϕ calculated from the two time-of-flight intensities

both high magnetic field and very cold neutrons: From Eq. (10.1) above, 30Å neutrons in a 1 T field precess 221 times every 1 mm flight path. If identical upstream and downstream field regions are used, the location where the π-flipping occurs will need to be accurate to 0.1 μm for a 10° accuracy. This would be a formidable task using currently available technology. However, only a small region that covers the sample will need the 1 T field. The rest of the field regions can use a field that can be substantially lower. This is because the spin precession angle depends upon both the field strength and the path length along which the field is imposed. A smaller field over a long distance can result in the same spin rotation as a larger field over a shorter distance. If a nominal 1 T field is applied over a 1 cm length where the sample is located and the rest of the setup is in a 20 gauss field, the second field region can extend 5 m and require an

accuracy of 0.06 mm in the π-flipping location for a 10° accuracy. The third challenge results from the fact that the precession of the neutrons starts at different locations along the beam. Hence either the downstream $\pi/2$ pulse or the π-flipping will need to be applied to different locations along the flight path. This would require a more sophisticated π-flipper setup than those currently used at neutron beam lines, which typically apply π-flipping over a small distance along the beam.

Hence although we have shown that spin contrast tomography is theoretically feasible, there are some interesting technical challenges to be overcome before the method can be applied in practice.

10.3 Prospects for Neutron-Probed Magnetic Resonance Imaging

Magnetic resonance imaging (MRI) is a powerful tool used primarily for internal imaging in biological systems. It is basically a position-dependent map of the nuclear spin relaxation time. There are many other systems that one would like to image using MRI, but they have a negligible penetration depth for radio frequency (RF) radiation. Therefore traditional MRI techniques cannot be used, and an alternative method to perform the nuclear magnetic resonance (NMR) measurement that is the core technology behind MRI must be found. The main classes of samples that are of interest are metallurgical samples, hydrogen storage materials, and biological samples in ionic salt solutions. As discussed elsewhere in this book, many of these systems can be addressed with conventional neutron radiography. Where MRI brings additional information is in systems where there are magnetic interactions of interest. For example in a magnetic alloy, MRI would provide a position-dependent measure of the interaction between one magnetic region and its environment, where conventional imaging only provides the positional dependence of the constituents of the alloy.

Neutrons are a promising probe to overcome the aforementioned difficulty. They penetrate deeply into materials. However, neutrons present their own challenges. Several of these are discussed. First and foremost is performing the NMR measurement.

Fundamentally, NMR and neutron spectroscopy are MHz and THz techniques, respectively. Therefore, although the Zeeman splitting of nuclear magnetic moments can be observed with conventional spectroscopy, the additional fine splittings of interest in NMR measurements cannot. Alternatively, a time-dependent measurement can be used to measure the decay of a nuclear spin (τ) and has been demonstrated in some limited cases. These studies used low temperature ($\sim$mK) [10], or microwaves [11], to saturate the nuclear spins. These oriented spins changed the intensity of Bragg peaks. Then studies the temperature was raised, or the microwaves turned off, and the intensity decay of the Bragg peak was recorded as a function of time. The resultant decay is proportional to τ. However, mK temperatures are difficult to attain, would

freeze liquid samples, and the microwaves suffer from the same penetration depth problems as the lower-frequency RF. An alternative approach to measuring the decay time must be found to make this technique accessible to more types of samples. A potential solution is to use high magnetic fields.

With the availability of high magnetic fields, a simple extension of the aforementioned techniques would be to use the field to raise the temperature necessary for the saturation of the nuclear spins. Figure 10.8 examines this possibility by looking at the nuclear polarization as a function of temperature for different fields. As can be seen from the figure, $T \sim 10$ mK is required for the current state of the art field for neutron-scattering experiments of 15 T. If the field was increased to 55 T, the required temperature is in the hundreds of mK range. Such an increase makes the measurement simpler but does not relieve the freezing problem. To use this technique at room temperature requires $\sim 10^5$ T, an unrealizable static field.

So the main challenge is to find another way to measure τ. The approach described below eliminates the need for microwaves and/or mK temperatures. The general idea is to use spectroscopy to measure the Zeeman splitting of relaxing nuclear spins at a high field, then quickly drop the field to a lower value and watch the Zeeman splitting relax to the equilibrium value at the lower field. A large static field is required to sufficiently separate the peak associated with the Zeeman splitting from other incoherent processes. Protons are the nuclei of choice for this study, as they are the most familiar NMR active nuclei. The protons are assumed to be provided by a water sample at room temperature. Therefore the nuclear relaxation time is assumed to be 200 ms. A static field of

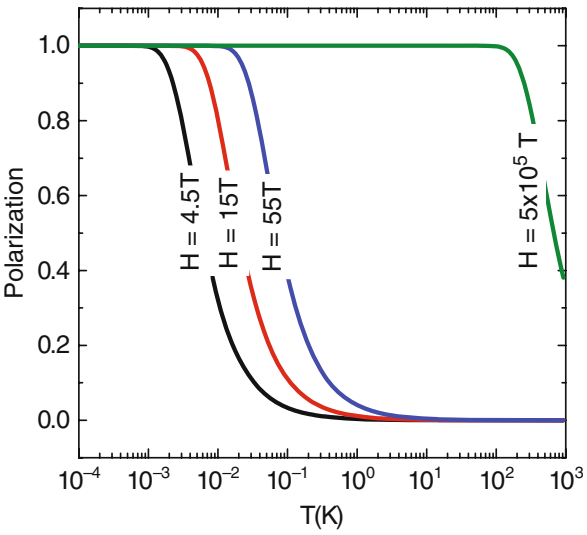

Fig. 10.8 The normalized proton polarization as a function of temperature for different values of magnetic field

15 T is sufficient for this system. Extending this technique to significantly more nuclei would require 2–4 times the static field, e.g., ~ 40 T [12]. The simulations detailed below are for a 10 T pulsed field on top of the 15 T static field.

To demonstrate the feasibility of this technique, one must show that, with current magnet technology, the field can cycle fast enough to allow for measurement of the nuclear relaxation time. The current state of the art in pulsed magnetic fields is the long-pulsed magnet at the National High Magnetic Field Laboratory in the United States [13]. A calculation was performed to observe the response of the resonance energy of the aforementioned proton system to a 10 T pulse (solid curve in Fig. 10.9) having the shape of the peak of the long pulse magnet [14]. The dashed curve is the resultant solution to the Bloch equation [15]. The equation was solved numerically with MathCAD [16]. This resonance energy will be the center value for the splitting of the scattering away from zero energy transfer. Given the dashed curve, a pulsed neutron source, operating at 60 Hz, will provide 80 pulses over the observed nuclear decay time.

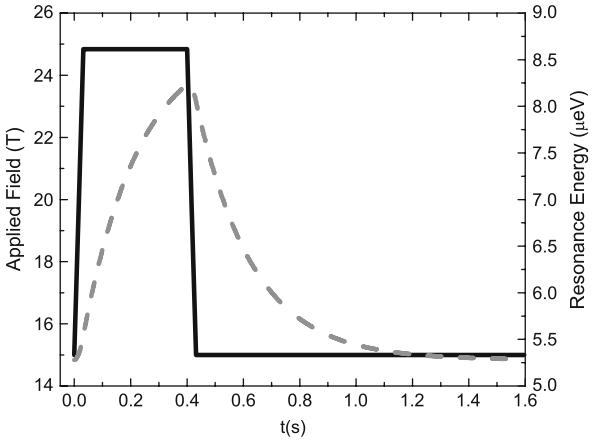

Fig. 10.9 The resonance energy for a system of hydrogen nuclei (*dashed curve*) for a given applied field (*solid curve*)

An estimate of the neutron count rate is also necessary to demonstrate the feasibility of this type of experiment. Approximations of the cross-sections for scattering between spin states were estimated elsewhere [17]. The assumed flux on a 40 mm^3 sample is of the order 10^5 n cm^{-2} s^{-1}. The scattering from the sample will illuminate 0.379 sr of detector area. The energy resolution of the instrument close to the elastic line is 3 μeV. (Detailed balance and absorption are ignored in these calculations.) Given these assumptions, an example trace is simulated and shown in the inset of Fig. 10.10. A similar trace is calculated every 16.7 ms out to 1.7 s after the field is applied. The uncertainty in the curve is simulated Poisson statistics. To obtain sufficient counting statistics, each point

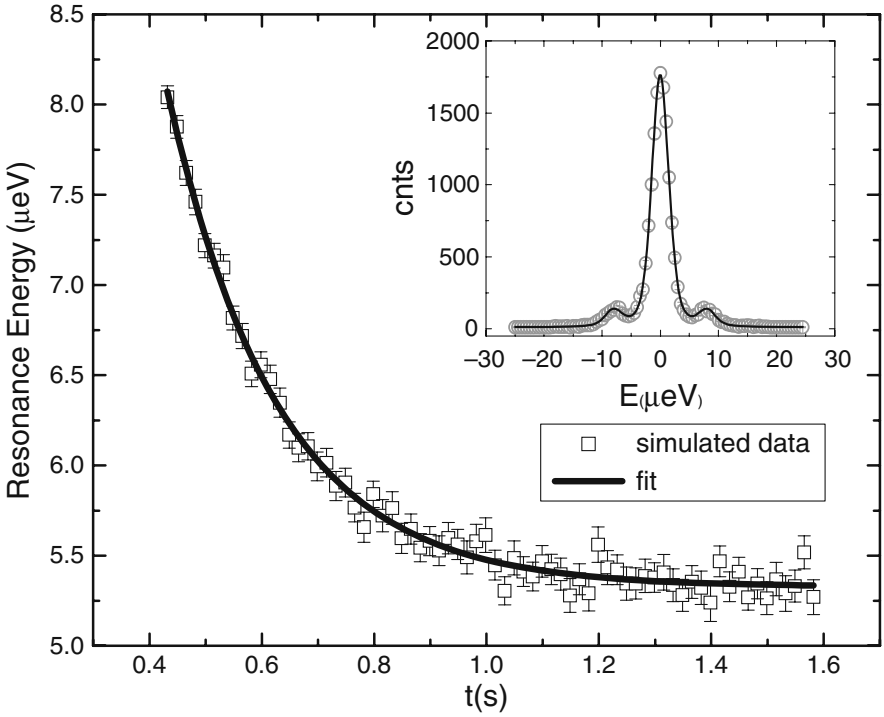

Fig. 10.10 The resonance energy determined from the simulated spectra. The resonance energy is fitted to an exponential decay to determine the relaxation time. The inset shows an example simulated spectrum (*circles*) and a fit (*solid*)

on the decay curve should be counted for a total of 10 s. Therefore the measurement would be repeated many times and the aggregated results analyzed. In practice this means a ~ 0.6 Hz pulsed magnet operated for 600 pulses. A full relaxation time measurement would require ~ 20 min.

Each of these resultant spectra are analyzed by fitting 3 Lorentzians of 1 μeV width, convoluted with the instrumental energy resolution of 3 μeV, at each time interval. The parameter to be tracked, as a function of time, to determine the relaxation time is the splitting of the finite energy transfer peaks from the center. The results from the simulated data for this parameter and its uncertainties are plotted as points in Fig. 10.10. An exponential decay is then fit to the points to determine the relaxation rate. The specific function used for this fit is $E = Ae^{-t/\tau} + E_0$ with E_0 the field splitting at the lower field value and A a normalization constant. The results are as follows: $\tau = 196 \pm 5$ ms, $A = 25 \pm 2$ μeV and $E_o = 5.33 \pm 0.02$ μeV. The fitted relaxation or Zeeman splitting time, τ, is in excellent agreement with the input time of 200 ms. Therefore, simulations show that neutron measurements of the relaxation time could be performed by watching the timed decay of the Zeeman splitting.

To test the limits of this method, similar calculations were performed with a 10 T static field. However, for this configuration the Zeeman splitting was too small at the longest times to be resolved from the central incoherent peak. This resulted in an artificially large value of τ from the fit. In principle the τ measurement will be influenced at longer times by the spins already flipped at shorter times. However, less than 10^6 spins are flipped before the next field pulse is applied, which is a negligible quantity when compared with the total number of spins in the system.

In order to do this measurement, a high-resolution spectrometer such as BASIS at the U.S. Spallation Neutron Source (SNS), a high (static) field magnet in excess of 30 T such as that proposed for Zeemans at the SNS, and a 10 T pulsed magnetic field are required [18, 19].

Though the core technology behind neutron-probed MRI has been described, other significant challenges remain. Position encoding is one of them. In traditional MRI a field gradient is placed across the sample [20, 21]. Then the resonance condition is only met at one spot in the sample. The field gradient is then varied to change this location. A field gradient would only smear out the neutron-probed measurement as it measures all energies. Instead, we would raster the sample through the beam so only a single-point is measured at a time. We assume the state of the art pixel size of 1×1 mm to 0.1×0.1 mm, as defined for the Vulcan instrument at SNS [22]. An additional restriction is that the bore in the proposed magnet [19] is only 50 mm. Therefore rastering a sample within this bore requires a small sample $\sim 1 \times 1$ cm and would provide between 100 and 10000 unique points depending on the beam size. Extending this technique to larger samples is a motivation for increasing the bore size in the next generation of superconducting hybrid magnets. Another approach would be to use small pulsed magnets that can achieve 30 T, but have a repetition rate of $\sim$1 pulse per 7–8 minutes [23]. A sample sandwiched between two of these magnets and rastered independently of the magnets provides a way to increase the sample size. For this approach one would have to stop measuring the relaxation after the peaks associated with the Zeeman splitting coalesce with the main incoherent peak. The main restriction of this approach is the long time between pulses. This time is controlled by internal heating of the magnet. The time between pulses could be reduced to the time limit of the capacitor bank power supply by rastering additional magnets while the first pair cools.

For both styles of magnets, field gradients are important. Though for traditional MRI homogeneity on a few PPM [20] is expected, $\sim$100 ppm is acceptable. The pulsed magnets are quite configurable so field gradients of this order are reasonable. For the Zeemans style of magnet, a high-homogeneity (100 ppm) resistive insert would have to be designed. This insert design would drop the peak field to $\sim$28 T (M. D. Bird, private communications). Nevertheless, one could envision running the magnet for a series of cycles in a high field mode and then changing for another series of cycles to a high homogeneity mode.

Finally, counting times for the MRI measurement must be considered. Assuming the counting described for the NMR measurement, but reducing the sample to a 1×1 mm cross-section, means that beam focusing of $\sim$15,000 is required so that a measurement can be carried out in 1 week. This is assuming that the static and pulsed field method is used. An order of magnitude may be gained by increasing the pulse rate of the pulsed magnet. If the fully pulsed field approach is used, this number would increase, as the repetition rate is even slower. Therefore beam flux is the biggest challenge to realizing neutron-probed MRI.

In summary the major challenges to realizing neutron-probed MRI are technical and not fundamental to the science. The core technique of neutron NMR can be demonstrated with the next generation of high magnetic field beamlines. Nevertheless, flux and the limitations on neutron focusing are the major challenges to using the neutron NMR technique for neutron-probed MRI.

Acknowledgments Garrett Granroth is grateful for useful discussions with J.-K. Zhao, G. Greene, E. Iverson, M. W. Meisel, N. Sullivan, and B. Halperin. His work was performed at Oak Ridge National Laboratory, managed for the U.S. Department of Energy by UT-Battelle, LLC, under Contract No. DE-AC05-00OR22725.

References

1. N. Kardjilov, I. Manke, M. Strobl, A. Hilger, W. Treimer, M. Meissner, T. Krist, J. Banhart, Three-dimensional imaging of magnetic fields with polarised neutrons, *Nat. Phys.* **4**, 399–403 (2008).
2. Th. Krist, S. J. Kennedy, T.J. Hick, F. Mezei, New compact neutron polarizer. *Physica B* **241–243**, 82–85 (1998).
3. W. Treimer, M. Strobl, N. Kardjilov, A. Hilgar, I. Manke, Wavelength turable device for neutron radiography and temography, *Appl. Phys. Lett*, **89**, 203504 (2006).
4. A. Hilger, N. Kardjilov, M. Strobl, W. Treimer, J. Banhart, The new cold neutron radiography and tomography instrument CONRAD at HMI Berlin, *Physica B* **385–386**, 1213 (2006).
5. P. Gammel, D. Bishop, Fingerprinting vortices with smoke, *Science* **279**, 410–411 (1998).
6. Ch. Jooss, J. Albrecht, H. Kuhn, S. Leonhardt, H. Kronmüller, Magneto-optical studies of current distributions in high-T_c superconductors. *Rep. Prog. Phys.* **65**, 651–788 (2002).
7. I. Manke, N. Kardjilov, M. Strobl, A. Hilger, J. Banhart, Investigation of the skin effect in the bulk of electrical conductors with spin-polarized neutron radiography, *J. Appl. Phys*, 104, 076109 (2008).
8. http://www.springer.com/series/8141, this series of books
9. A.I. Frank, I. Anderson, I.V. Bondarenko, A.V. Kozlov, P. Hoghoj, and G. Ehlers, *Phys. Atom. Nucl.* **65**, 2009 (2002).
10. T.A. Jyrkkiö, M.T. Huiku, K.N. Clausen, K. Siemensmeyer, K. Kakurai, and M. Steiner, Calibration and applications of polarized neutron thermometry at milli- and microkelvin temperatures, *Z. Phys. B* **71**, 139 (1988).
11. J.B. Hayter, G.T. Jenkin, and J.W. White, Polarized-Neutron Diffration from Spin-Polarized Protons: A Tool in Structure Determination? *Phys. Rev. Lett.* **33**, 696 (1974).
12. M. Dobhal, *NMR Data for Carbon-13. Part 4: Natural Products*, Springer, Heidelberg (2006).

13. http://www.lanl.gov/orgs/mpa/nhmfl/60TLP.shtml
14. http://www.lanl.gov/orgs/mpa/nhmfl/images/60TLPpulse.jpg
15. C.P. Slichter, *Principles of Magnetic Resonance*, Springer-Verlag, Heidelberg (1990).
16. MathCad, Parametric Technology Corporation.
17. G.E. Granroth, *Prospects for Neutron probed NMR* in The proceedings of ICANS–XVII, J. Wei, S. Wang, W.L. Huang, J.S. Zhao, ed. http://www.icans-xviii.ac.cn/proceedings/indexed/copyr/15. pdf.
18. http://www.sns.gov/instrument_systems/beamline_02_basis/index.shtml, (2007).
19. G.E. Granroth, C. Broholm, F. Klöse, G. Srajer, Z. Islam, Y. Lee, and J. Lang, *Report from Probing Matter at High Magnetic Fields with X-Rays and Neutrons*, SNS Report SNS107000000TR-005-R00, (2005).
20. J. Jin, *Electromagnetic Analysis and Design in Magnetic Resonance Imaging*, CRC Press, Boca Raton (1999).
21. P. Sprawls, *Magnetic Resonance Imaging*, Medical Physics Publishing, Madison (2000).
22. X.-L. Wang, T.M. Holden, G.Q. Rennich, A.D. Stoica, P.K. Liaw, H. Choo, and C.R. Hubbard, *Physica B* **385–386**, 673 (2006).
23. K. Ohoyama, N. Katoh, H. Nojiri, Y.H. Matsuda, H. Hiraka, K. Ikeda, H.M. Shimizu, Neutron diffraction under 30 T pulsed magnetic fields, *J. Mag. Mag. Mat.* **310**, e974 (2007).